MEMS-Based Flexible Force Sensor for Tri-Axial Catheter Contact Force Measurement

Hardik J. Pandya,

Department of Medicine in the Brigham and Womens Hospital – Harvard Medical School, Boston, MA 02115, USA

Jun Sheng, and

Medical Robotics and Automation Laboratory (RoboMed) in the Wallace H. Coulter Department of Biomedical Engineering, Georgia Institute of Technology, Atlanta, GA 30332, USA

Jaydev P. Desai [Senior Member, IEEE]

Medical Robotics and Automation Laboratory (RoboMed) in the Wallace H. Coulter Department of Biomedical Engineering, Georgia Institute of Technology, Atlanta, GA 30332, USA

Abstract

Atrial fibrillation (AFib) is a significant healthcare problem caused by the uneven and rapid discharge of electrical signals from pulmonary veins (PVs). The technique of radiofrequency (RF) ablation can block these abnormal electrical signals by ablating myocardial sleeves inside PVs. Catheter contact force measurement during RF ablation can reduce the rate of AFib recurrence, since it helps to determine effective contact of the catheter with the tissue, thereby resulting in effective power delivery for ablation. This paper presents the development of a three-dimensional (3D) force sensor to provide the real-time measurement of tri-axial catheter contact force. The 3D force sensor consists of a plastic cubic bead and five flexible force sensors. Each flexible force sensor was made of a PEDOT:PSS strain gauge and a PDMS bump on a flexible PDMS substrate. Calibration results show that the fabricated sensor has a linear response in the force range required for RF ablation. To evaluate its working performance, the fabricated sensor was pressed against gelatin tissue by a micromanipulator and also integrated on a catheter tip to test it within deionized water flow. Both experiments simulated the ventricular environment and proved the validity of applying the 3D force sensor in RF ablation.

I. Introduction

Atrial fibrillation (AFib) is an irregular heartbeat (arrhythmia) which is caused by uneven and rapid discharge of electrical signals from pulmonary veins (PVs) and can lead to various heart-related complications. According to American Heart Association, estimated 2.7 million Americans are living with AFib and studies show that the AFib prevalence will be projected to 12.1 million cases by 2030 [1]. Radiofrequency (RF) ablation is a treatment technique which can electrically isolate PVs from the left atrium (LA) [2]–[5]. Despite achieving PVs isolation, the recurrence of AFib is common after RF ablation and the

Correspondence to: Hardik J. Pandya.

recovery of left atrial PVs conduction was found in patients during follow-up studies [6]–[8]. The main challenge for proper RF ablation is to ensure the full-thickness scar formation to achieve long-lasting PVs isolation [4], [9], [10]. To achieve transmural lesions, sufficient RF ablation energy needs to be delivered to the local tissue to minimize the excitable tissue recovery [11], [12]. Apart from RF ablation energy, lesion formation is dependent on several other variables including catheter tip size, orientation, duration of ablation, and catheter contact force [13]–[15]. Studies have shown that catheter contact force is an important determinant of lesion size for over 20 years [16]–[20], yet only recently the tip-to-tissue contact force in real-time was studied [21]–[24]. Data from the studies suggest that an RF ablation catheter guided by contact force requires one third less fluoroscopy, has higher success rates, and is faster compared with its standard counterparts [21]–[24].

The fundamental function of the contact force sensor for an RF ablation catheter is to detect normal and tangential forces and few studies have been carried out to fabricate such force sensors [25]–[30]. Some important parameters for contact force sensors include thickness, flexibility, sensitivity, and mass-fabrication capabilities. Soft materials like Polydimethylsiloxsane (PDMS), Poly(methyl methacrylate) (PMMA), conductive rubber were used to skirt these aspects and simplify fabrication approaches [25]–[27], [30]. In all these techniques, though the force sensor can be miniaturized, the packaging makes the whole system bulky. The capacitive sensing force sensor shows high sensitivity and resolution but requires a signal conditioning unit closer to the sensor to avoid parasitic capacitance [29], [31].

A strain gauge can act as a force sensor as its electrical characteristics change with mechanical deformation. The parameters like sensitivity (i.e., gauge factor (GF)), stretchability, fabrication cost, the speed of response, and stability are governing factors for high-performance force sensors. Conventional strain gauges require low fabrication cost but have poor stretchability and sensitivity [32], [33]. In the biomechanics, physiology, and kinesiology applications, stretchable and sensitive force sensors capable of accommodating large strain are required [34]. Research has been carried out on miniaturized sensors such as the tri-axial force sensor on a surgical scalpel [35], the catheter with tactile sensing for RF ablation [36], [37], and the array of pressure sensors to obtain the information of the catheter in contact with vascular vessels [38].

PDMS elastomer has high oxygen and low water permeability, and is an inert biocompatible elastomeric material [39]. PDMS is also used as a structural material for fabricating force sensors due to its flexibility and biomedical compliance with human tissue [40], [41]. Besides, the Young's modulus of a PDMS substrate can be less than 1/1000 of that of a Kapton substrate [42] and a PDMS substrate can be as flexible as human skin [41]. Therefore, PDMS is a better choice as the substrate of flexible force sensors. Poly(3,4-ethylenedioxythiophene) (PEDOT) polymer has thermal and electrochemical stability, high electrical conductivity, and transparency. As this polymer is insoluble, it is available in its oxidized form in combination with polystyrene sulfonic acid (PSS) (water-soluble polymer). Combining PSS to PEDOT causes the attachment of PEDOT segments to the long chains of PSS and allows the dispersion of PEDOT in water [43]. The PEDOT:PSS conducting

polymer has a wide range of applications from antistatic coating, electronic, optoelectronic devices [44], humidity sensors [45], and strain sensors [46], [47].

In this work, we present the design and fabrication of a novel three-dimensional (3D) force sensor for tri-axial contact force measurement, which can be integrated on a catheter. A conceptual diagram of a catheter integrated with the 3D force sensor for measuring contact force applied by tissue around PVs is shown in Fig. 1. The 3D force sensor consists of a plastic cubic bead with each of its five sides integrated with a flexible force sensor, which was made of a PEDOT:PSS strain gauge and a PDMS bump on a flexible PDMS substrate, so the 3D force sensor is capable of measuring tri-axial contact force simultaneously. To characterize the fabricated 3D force sensor, it was tested under varying compressive force exerted by a micromanipulator via a plastic stick. To understand the influence of the force exerted by soft tissue and flowing liquid, the fabricated 3D force sensor was pressed against the phantom tissue made from gelatin and immersed within flowing deionized water while the output voltage was measured. The schematic diagram of the 3D force sensor is shown in Fig. 2(a) and its fabrication processes are illustrated in Figs. 2(b) to (d).

II. Materials and Methods

A. Sensor Fabrication

The flexible force sensor was fabricated on a PDMS polymer substrate and a three-mask process was used in its fabrication. The process flow for its fabrication is shown in Fig. 2(b) and described as follows: (i) Silicon (Si) wafer (4 inch diameter and 550 μm thickness) was used as the substrate which provided structural support during fabrication; (ii) Silicon dioxide (SiO$_2$, 0.5 μm thickness) was grown on the silicon wafer. PDMS (SYLGARD® 184, Sigma-Aldrich, USA) (200 μm thickness) was spin-coated on the wafer and cured at 125 °C for 25 minutes. The thickness of the PDMS layer, ranging from hundreds of microns down to a few microns, could be controlled easily by the spin speed. Then, PEDOT:PSS (0.5 μm thickness) was spin-coated on the PDMS layer and silver (Ag) film (0.1 μm thickness) was deposited over the PEDOT:PSS film as a protective layer. Another protective layer for PEDOT:PSS could be parylene, but there would be a risk of damage to the surface of the PEDOT:PSS film when parylene is etched at the end of the process; (iii and iv) Positive photoresist (PR) was spin-coated on the Ag/PEDOT:PSS film and patterned using soft contact photolithography (Mask 1). Due to the mismatch of the coefficient of thermal expansion (CTE) between PDMS and PR, rapid temperature change may result in cracks in the PR layer. To avoid the cracking, the PR layer after coating was settled down for 6 minutes and baked in an oven for 1 minute at 60 °C before UV exposure. The exposed silver was etched with silver etchant followed by oxygen plasma etching of PEDOT:PSS. Then, the PR layer is stripped off and the silver on the patterned PEDOT:PSS film is etched to form a PEDOT:PSS strain gauge; (v) Cr/Au (0.02 μm / 0.5 μm thickness) film was deposited using e-beam evaporation and patterned using lift-off technique to form the contact pads for the strain gauge (Mask 2). A PDMS bump (2200 μm $\times$ 2200 μm $\times$ 900 μm, L $\times$ W $\times$ H) was fabricated separately as shown in Fig. 2(c). After processing the surfaces of the PDMS substrate and PDMS bump in the ICP Oxygen plasma for 40s at 50W and 1 Torr pressure, the PDMS bump was aligned with the strain gauge at their respective centers using an

optical microscope (Leica Microsystems®) and pressed on the PDMS substrate for 60s followed by heating the device at 90 °C for 2 minutes to achieve successful bonding; (vi) The PDMS substrate was peeled off from the oxidized silicon wafer to realize the flexible force sensor.

The process flow for fabricating the PDMS bump, as shown in Fig. 2(c), includes the following steps: (i) Si wafer (4 inch diameter and 550 μm thickness) was used as the base; (ii) SiO$_2$ (0.5 μm thickness) was grown on the Si wafer, patterned using photolithography (Mask 3), and etched using reactive ion etching (RIE), followed by Si etching using deep reactive ion etching (DRIE) to create a 400 μm deep pit (2200 μm $\times$ 2200 μm, L $\times$ W); (iii) PDMS was spin-coated on the wafer and cured at 125 °C for 15 minutes; (iv) The PDMS layer was released from the wafer to realize a PDMS bump. The total height of the bump is 900 μm (400 μm from the pit and 500 μm as the surface thickness). The selected PDMS curing temperature was close to the median of the recommended range [48], such that the fabricated PDMS bump was not too rigid, which would result in the easy breakage of the strain gauge, or too soft, which would result in the low sensitivity.

A plastic cubic bead made of VeroWhite material using a 3D printer (Objet Eden350V®, Stratasys, USA) with the dimension of 4000 μm $\times$ 4000 μm $\times$ 4000 μm (L $\times$ W $\times$ H) was used for fabricating the 3D force sensor. SiO$_2$ (1 μm thickness) was deposited on all the sides of the bead using the technique of plasma enhanced chemical vapor deposition (PECVD) and five fabricated strain gauges with PDMS pumps were attached on the individual sides to realize the 3D force sensor as shown in Fig. 2(d). The size of the active area for each flexible force sensor is 2000 μm $\times$ 2000 μm $\times$ 1100 μm (L $\times$ W $\times$ H). Figs. 3(a) to (c) show the SEM images of the fabricated flexible force sensor with and without the PDMS bump and the 3D force sensor, respectively.

B. Sensitivity Analysis

Normal force applied on the strain gauge deforms the gauge pattern and changes its electrical resistance. An ideal force sensor should be highly sensitive to external load, which means a relatively large change in electrical resistance under a certain amount of normal force. To validate our gauge pattern design made of square spirals shown in Fig. 4 (left), we compare it with another pattern design made of circular spirals shown in Fig. 4 (right) in terms of sensitivity, which was adopted for pressure sensing based on microchannels and liquid conductors by Yong-Lae Park's group *et al.* [49]. Several assumptions are made: (1) In the force free state, both patterns have the same material length (L_0) and same segment width (b), resulting in the same planar area; (2) In the force free state, both patterns have the same distance (d) between neighbouring pattern segments; (3) The electrical resistance of the gauge pattern exclusively depends on the length of the patterned material. In their schematic diagrams, pattern (i) has a square area with a side length of D, leading to $L_0 =$ 11D and $d = D/9$. To keep a uniform d, pattern (ii) adopts a pair of Archimedean spirals (S_a and S_b) and their parameterized equations are given by:

$$\begin{aligned} x(\theta) &= a\theta cos(\theta) \\ y(\theta) &= a\theta sin(\theta) \end{aligned} \quad (1)$$

where S_a: $\theta \in [0, \theta_0]$, S_b: $\theta \in [\pi, \theta_0 + \pi]$, and they denote two circular spirals with a phase shift of π. a determines the speed of the locus moving away from the origin point and θ_0 represents the span of the two spirals. The fact that the distance between neighbouring spiral coils is d yields: $a = d/\pi$. The material length of pattern (ii) before deformation is given by:

$$L_0 = \int_{S_a + S_b} \sqrt{dx^2 + dy^2} \quad (2)$$

By making $L_0 = 11D$ to satisfy the assumption (1), θ_0 is solved as 5.6π. The sensitivity of a strain gauge for tensile strain measurement is equal to the ratio of the relative resistance change to the tensile strain. Therefore, the sensitivity of a strain gauge for normal force measurement can be defined as the ratio of the relative resistance change to the normal pressure, which is given by:

$$GF = \frac{\Delta R_e / R_e}{p} = \frac{L_d - L_0}{p L_0} \quad (3)$$

where R_e is the value of electrical resistance in the force free state, R_e is change of electrical resistance when normal force is applied, p is the uniform normal pressure on the sensor, and L_d is the length of gauge pattern in the deformed state. Based on assumptions (1) and (2), the indent shapes on the PDMS substrates caused by normal force are assumed to be the same for patterns (i) and (ii). This is verified via simulation in SolidWorks by applying 0.2 MPa pressure on the active area of modeled force sensors without PDMS bumps, as shown in Fig. 5. The view of the cross section through the indent vertex indicates that the indent can be modeled as a paraboloid. By defining R as the indent radius on the surface of the bump, the parameterized equation for the indent model is given by:

$$x'(u, v) = R \sqrt{1 + u/H} \cos(v)$$
$$y'(u, v) = R \sqrt{1 + u/H} \sin(v)$$
$$z'(u, v) = u \quad (4)$$

where

$$u \in [-H, 0] \text{ and } v \in [0, 2\pi)$$

where R is the paraboloid radius on the surface of the PDMS substrate and H is the depth of the paraboloid at its vertex, as shown in Fig. 6. It is assumed that R is equal to $\sqrt{2}D/2$ for pattern (i) and $a\theta_0$ for pattern (ii) to cover the gauge pattern with the least value of R. The deformation of the strain gauge under normal force can be regarded as a process of projecting each point ($P(x, y)$) of the gauge pattern from a planar surface to a point ($P'(x', y', z')$) on the paraboloid by a nonlinear transformation. Since the applied force is normal, the projection does not cause displacement in $x - y$ plane, so the vertical displacement of P' can be derived from Eq. (4) as:

$$z' = H(x^2+y^2)/R^2 - H \quad (5)$$

The length of each pattern before and after deformation can be respectively calculated by:

$L_0 = \int_S \sqrt{dx^2+dy^2}$ and $L_d = \int_{S'} \sqrt{dx'^2+dy'^2+dz'^2}$, where S pand S' are the collections of points P and P' on the planar surface and paraboloid, respectively. By applying p from 0 MPa to 0.2 MPa with an equal interval of 50 kPa in simulation to obtain the simulated values of H, the values of analytical sensitivity for patterns (i) and (ii) (GF_i and GF_{ii}, respectively) are calculated and shown in Table I. The results show that pattern (ii) has a much lower sensitivity than pattern (i), because the circular spirals are close to the contours of the paraboloid and the length change caused by the normal deformation is very limited. Pattern (i) has relatively high sensitivity, because each of its straight segments bends to a parabola after the normal deformation.

C. Experimental Setup

Fig. 7 shows the schematic diagram of the calibration setup for the fabricated 3D force sensor. The setup primarily consists of a commercial micromanipulator (MP-285, Sutter Instrument®, USA), a commercial load cell (MLP-10, Transducer Techniques, USA), and a plastic stick with a flat tip. During calibration, the stick was actuated by the micromanipulator to normally press the PDMS bump of each flexible force sensor with three maximum displacements (400 μm, 600 μm, and 900 μm), resulting in the resistance change of the strain gauge. Each strain gauge was connected in an individual Wheatstone bridge circuit, such that the resistance change can be converted to voltage output, which was amplified by an instrumentation amplifier and collected by a data acquisition card (DAQ, Model 626, Sensoray, USA). Since all the strain gauges work independently, the crosstalk among the sensors does not need to be considered. A voltage follower circuit was used for the effective isolation of the output from the signal source and to avoid the loading effect. The system diagrams are shown in Fig. 8 and the calibration results for a typical flexible force sensor are shown in Fig. 9. The relationship between the force measured by the commercial load cell and the voltage output by the flexible force sensor is almost linear when the compressive force is between 0g to 40g and the R-square value in this linear range is equal to 0.9979. To create transmural lesions and avoid the risks of excessive tissue heating and AFib recurrence, the recommended pressing force applied to tissue in RF ablation is between 20g to 30g [50]. Therefore, the fabricated force sensor is capable of monitoring the catheter contact force in the RF ablation surgery.

To investigate the influence of soft tissue on the fabricated 3D force sensor, the phantom tissue made from 12% by weight Knox gelatin (Kraft Foods Global, Inc., USA) was prepared. To characterize its stiffness, the gelatin slab was vertically indented by 6 mm by an aluminum stick with a parabolic tip under the actuation of the micromanipulator as shown in Fig. 10(a). Meanwhile, the reaction force during the indentation process was measured by the commercial load cell. Based on the Hertz model [51] and Matlab® Curve Fitting Toolbox™, the stiffness of the gelatin tissue was calibrated to be 19.8 kPa, which was close

to the passive stiffness of normal heart muscles [52]. Then, the aluminum stick was replaced by a plastic stick integrated with the fabricated 3D force sensor on its tip as shown in Fig. 10(b). By moving the micromanipulator downward, the flexible force sensor on the bottom can press the gelatin tissue. When the sensor output voltage was measured in this process, the contact force was also measured by the commercial load cell. Since the flexible force sensors are similar when they are individually actuated to press the gelatin surface, we only tested the flexible force sensor on the bottom.

To evaluate the working performance of the fabricated 3D force sensor within simulated blood flow, the sensor was integrated with a commercial catheter (Coloplast SpeediCath® on its tip and placed inside a tube (10 mm inner diameter, similar to the diameter of PVs [53]) with deionized water flowing through the tube, as shown in Fig. 11. Duct tape was used to seal the entry hole on the tube wall after the catheter was inserted. Experiments were carried out to calibrate the relationship between the voltage applied to the water pump (DC50C-2465A, ZKSJ Co., Ltd) and the flow rate. The dynamic pressure (p) for incompressible fluid is given by: $p = \frac{1}{2} \rho v^2$ [54], where ρ and v represent the fluid density and flowing speed, respectively. By assuming water to be incompressible, three flow rates (2.1 L/min, 3.5 L/min, and 5.2 L/min) were selected to simulate the normal blood pressure within PVs in the left atrium [55]. The estimated compressive force applied on the top of the PDMS bump that faces the water flow is around 0.2g if the flow rate is equal to 5.2 L/min, which is much smaller than the contact force applied by the soft tissue. Hence, a high amplification gain and a low-pass filter circuit were used to amplify the output voltage and reduce noise. At each flow rate, two experiments were individually performed and the water flow was supplied by the water pump for 10s followed by a rest period of 10s in each experiment.

III. Results and Discussion

The 3D force sensor with PDMS bumps was simulated in SolidWorks by applying 0.5N normal force on the PDMS bump of each flexible force sensor. In the simulation, the monomeric units of the elastomer (PDMS) that are tangled with each other get strained. These tangled chains reconfigure themselves to distribute the applied force which contributes to the bending of the PDMS substrate. The displacement of the membrane and the stress distribution are shown in Fig. 12.

In the gelatin tests, the performance of the flexible force sensor was compared between with and without the PDMS bump when the bottom flexible force sensor was pressed against the gelatin tissue. In each experiment, the micromanipulator moved at the speed of 50 μm/s for 100s followed by a retrieve period of another 100s. Fig. 13 shows that the flexible force sensor with the PDMS bump relatively precisely measured the contact force applied by the gelatin tissue based on the previous calibration results with the root-mean-square error (RMSE) equal to 0.8896g. Fig. 14 shows that the flexible force sensor without the PDMS bump reached an output saturation quickly and failed to measure the contact force. This is because that when the gelatin tissue was pressed by the sensor without the bump, a paraboloidal concave was formed on the gelatin surface, resulting in a gap between the gelatin and the strain gauge. Therefore, the contact force was primarily applied on the

contact pads and the surrounding inactive area, rather than the strain gauge. When the PDMS bump was used, the gap was filled by the bump and the contact force was continuously applied on the strain gauge via the PDMS bump during the pressing process.

In the evaluation tests within deionized water flow, the responses of all the five flexible force sensors are shown in Figs. 15(a) to (e). The resistance change of the flexible force sensor was a synthetic result of the water electroconductivity and the compression by the water flow. Fig. 15(f) shows that the output voltage decreased when the sensor was manually immersed into the still water at 10s, because the total electrical resistance decreased when the water acted as an additional resistance in parallel to the strain gauge. Compression by the water flow on the top and sides of the sensor bump can increase and decrease the sensor resistance, respectively, and it is assumed that the pressure applied on the bump surface facing the water flow is much higher than the pressure on other surfaces. When the water flow was supplied, the resistance decrease caused by the water electroconductivity was the dominant factor, so the output voltage decreased, as shown in Figs. 15(a) to (e). For the front sensor, the compressive force applied on the top of the PDMS bump increased when the flow rate became higher, causing the increase of the output voltage, as shown in Fig. 15(a). For the rear sensor, strong turbulence occurred when the flow rate was 5.2 L/min, causing a smaller compressive force on the top of the PDMS bump and a decreased output voltage, as shown in Fig. 15(b). As shown in Figs. 15(c) to (e), the increase of the output voltage for the bottom, left, and right sensors at higher flow rates was limited, probably because the area of the side of the bump was very small. Due to the high amplification gain and the limited resolution of the potentiometer, it was difficult to set the initial output voltage to be zero and the value varied among individual tests. To reduce the influence of the electroconductivity of blood and tissue liquid on the sensor reading in a real circumstance, the PEDOT:PSS strain gauge can be further insulated by using a polyester resin (Bectron® DP 8401 VP, Elantas Beck) [56].

IV. Conclusion

The presented work shows the design, fabrication, and application of a 3D force sensor to measure the tri-axial catheter contact force. The device is not only simple to fabricate but also small enough to be integrated on the catheter tip. The 3D force sensor is composed of a plastic cubic bead and five flexible force sensors integrated on the sides of the bead. Each flexible force sensor was fabricated using existing microfabrication technologies. PDMS and PEDOT:PSS were used as the substrate and sensing material, respectively. The fabricated flexible force sensor has a relatively large linear measurement range which is promising for the contact force measurement in RF ablation. To evaluate the fabricated 3D force sensor, it was pressed against the gelatin tissue with stiffness similar to the heart muscles by a micromanipulator. A commercial catheter integrated with the fabricated 3D force sensor was placed inside deionized water flow to measure the response of all the flexible force sensors. In our future work, our focus would be on the further miniaturization of the sensor, sensitivity improvement, and fabrication of an array of flexible force sensors. We also plan to improve the design of the flexible force sensor to increase its linear measurement range. In addition, we are envisioning integrating the sensor array on a steerable robotic catheter

and measure small contact force within an environment mimicking the ventricular and vascular system.

Acknowledgments

Biographies

Hardik J. Pandya is currently a postdoctoral research fellow in the Department of Medicine at Brigham and Women's Hospital – Harvard Medical School. Prior to joining Harvard, he was a postdoctoral research associate (July 2014 – January 2016) and faculty research assistant (September 2012 – June 2014) in the Department of Mechanical Engineering at the University of Maryland, College Park. He received his Ph.D. with major in MEMS-based sensors technology from IIT Delhi in November 2013 and his graduate (April 2002) and postgraduate (April 2004) degrees in Electronics from Sardar Patel University (SPU), Gujarat, India. He was bestowed with the university gold medal in his post graduation studies. Prior to joining his Ph.D. studies, he worked as a lecturer (August 2006 – February 2009) in the Department of Electronics and Communication Engineering at Invertis Institute of Engineering and Technology. His research interest is integrating biology/medicine with micro- and nanotechnology to develop innovative tools to solve unmet clinical problems. His interests also include design and fabrication of microsensors for cancer diagnosis, additive manufacturing for microsensor packaging, flexible sensors and devices for biomedical robotics, and MEMS-based sensors for VOC sensing. He has been a co-inventor in an Australian patent, has filed two US patent, and three Indian patents in the area of biosensors, MEMS-based sensors for cancer diagnosis, and energy-efficient VOC sensors. His work has been published in high-quality journals such as Lab on a Chip, IEEE Transactions on Biomedical Engineering, Sensors and Actuators B, Biosensors and Bioelectronics, and Journal of Micromechanics and Micromachining.

Jun Sheng earned his Bachelor of Science in Mechanical Engineering from Shanghai Jiao Tong University, Shanghai, China, in 2011. He also received his Master of Science in Electrical Engineering from National Taiwan University, Taipei, Taiwan, in 2013. He is currently working towards his Ph.D degree in Robotics in the Wallace H. Coulter Department of Biomedical Engineering at Georgia Institute of Technology (Georgia Tech). His research interests include design, fabrication, and control of surgical robots and biomedical devices.

Jaydev P. Desai is currently a Professor and BME Distinguished Faculty Fellow in the Wallace H. Coulter Department of Biomedical Engineering at Georgia Institute of Technology (Georgia Tech). Prior to joining Georgia Tech, he was a Professor at University of Maryland, College Park (UMCP). He completed his undergraduate studies from the Indian Institute of Technology, Bombay, India, in 1993. He received his M.A. in Mathematics in 1997, M.S. and Ph.D. in Mechanical Engineering and Applied Mechanics in 1995 and 1998 respectively, all from the University of Pennsylvania. He was also a Post-Doctoral Fellow in the Division of Engineering and Applied Sciences at Harvard University from 1998–1999. He is a recipient several NIH R01 awards, NSF CAREER award, and was also the lead inventor on the Outstanding Invention of 2007 in Physical Science Category at UMCP. He is also the recipient of the Ralph R. Teetor Educational Award. He was an invited speaker at the National Academy of Sciences Distinctive Voices seminar series and also invited to attend the National Academy of Engineering U.S. Frontiers of Engineering Symposium. His research interests include surgical robotics, MEMS-based cancer diagnosis, micro-scale cell and tissue characterization, haptics, and grasping. He is also a fellow of the ASME and senior member of the IEEE.

References

1. Colilla S, Crow A, Petkun W, Singer DE, Simon T, Liu X. Estimates of current and future incidence and prevalence of atrial fibrillation in the us adult population. The American journal of cardiology. 2013; 112(8):1142–1147. [PubMed: 23831166]
2. Jai P, Hai M, Shah DC, Chouairi S, Gencel L, Cle J, et al. A focal source of atrial fibrillation treated by discrete radiofrequency ablation. Circulation. 1997; 95(3):572–576. [PubMed: 9024141]

3. Haissaguerre M, Jaïs P, Shah DC, Takahashi A, Hocini M, Quiniou G, Garrigue S, Le Mouroux A, Le Métayer P, Clémenty J. Spontaneous initiation of atrial fibrillation by ectopic beats originating in the pulmonary veins. New England Journal of Medicine. 1998; 339(10):659–666. [PubMed: 9725923]

4. Jaïs P, Weerasooriya R, Shah DC, Hocini M, Macle L, Choi K-J, Scavee C, Haïssaguerre M, Clémenty J. Ablation therapy for atrial fibrillation (AF). Cardiovascular research. 2002; 54(2):337–346. [PubMed: 12062339]

5. Pappone C, Rosanio S, Oreto G, Tocchi M, Gugliotta F, Vicedomini G, Salvati A, Dicandia C, Mazzone P, Santinelli V, et al. Circumferential radiofrequency ablation of pulmonary vein ostia a new anatomic approach for curing atrial fibrillation. Circulation. 2000; 102(21):2619–2628. [PubMed: 11085966]

6. Rajappan K, Kistler PM, Earley MJ, Thomas G, Izquierdo M, Sporton SC, Schilling RJ. Acute and chronic pulmonary vein reconnection after atrial fibrillation ablation: a prospective characterization of anatomical sites. Pacing and clinical electrophysiology. 2008; 31(12):1598–1605. [PubMed: 19067813]

7. Weerasooriya R, Khairy P, Litalien J, Macle L, Hocini M, Sacher F, Lellouche N, Knecht S, Wright M, Nault I, et al. Catheter ablation for atrial fibrillation: are results maintained at 5 years of follow-up? Journal of the American College of Cardiology. 2011; 57(2):160–166. [PubMed: 21211687]

8. Cappato R, Negroni S, Pecora D, Bentivegna S, Lupo PP, Carolei A, Esposito C, Furlanello F, De Ambroggi L. Prospective assessment of late conduction recurrence across radiofrequency lesions producing electrical disconnection at the pulmonary vein ostium in patients with atrial fibrillation. Circulation. 2003; 108(13):1599–1604. [PubMed: 12963643]

9. Swartz J. A catheter-based curative approach to atrial fibrillation in humans. Circulation. 1994; 90:I–335.

10. Jaıs P, Shah DC, Haıssaguerre M, Takahashi A, Lavergne T, Hocini M, Garrigue S, Barold SS, Le Métayer P, Clémenty J. Efficacy and safety of septal and left-atrial linear ablation for atrial fibrillation. The American journal of cardiology. 1999; 84(9):139–146.

11. Hutchinson MD, Garcia FC, Mandel JE, Elkassabany N, Zado ES, Riley MP, Cooper JM, Bala R, Frankel DS, Lin D, et al. Efforts to enhance catheter stability improve atrial fibrillation ablation outcome. Heart Rhythm. 2013; 10(3):347–353. [PubMed: 23128019]

12. Reichlin T, Michaud GF. Our approach to maximizing the durability of pulmonary vein isolation during a paroxysmal atrial fibrillation ablation procedure. Journal of cardiovascular electrophysiology. 2012; 23(11):1272–1276. [PubMed: 22913515]

13. Wittkampf FH, NAKAGAWA H. Rf catheter ablation: Lessons on lesions. Pacing and Clinical Electrophysiology. 2006; 29(11):1285–1297. [PubMed: 17100685]

14. Kuck K-H, Reddy VY, Schmidt B, Natale A, Neuzil P, Saoudi N, Kautzner J, Herrera C, Hindricks G, Jaïs P, et al. A novel radiofrequency ablation catheter using contact force sensing: Toccata study. Heart Rhythm. 2012; 9(1):18–23. [PubMed: 21872560]

15. Avitall B, Mughal K, Hare J, Helms R, Krum D. The effects of electrode-tissue contact on radiofrequency lesion generation. Pacing and clinical electrophysiology. 1997; 20(12):2899–2910. [PubMed: 9455749]

16. Haines DE. Determinants of lesion size during radiofrequency catheter ablation: The role of electrode-tissue contact pressure and duration of energy delivery. Journal of Cardiovascular Electrophysiology. 1991; 2(6):509–515.

17. Strickberger SA, Vorperian VR, Man KC, Williamson BD, Kalbfleisch SJ, Hasse C, Morady F, Langberg JJ. Relation between impedance and endocardial contact during radiofrequency catheter ablation. American heart journal. 1994; 128(2):226–229. [PubMed: 8037086]

18. Zheng X, Walcott GP, Hall JA, Rollins DL, Smith WM, Kay GN, Ideker RE. Electrode impedance: an indicator of electrode-tissue contact and lesion dimensions during linear ablation. Journal of Interventional Cardiac Electrophysiology. 2000; 4(4):645–654. [PubMed: 11141212]

19. Nath S, DiMarco JP, Gallop RG, McRury ID, Haines DE. Effects of dispersive electrode position and surface area on electrical parameters and temperature during radiofrequency catheter ablation. The American journal of cardiology. 1996; 77(9):765–767. [PubMed: 8651132]

20. Eick OJ, Wittkampe FH, Bronneberg T, Schumacher B. The letr-principle: A novel method to assess electrode-tissue contact in radiofrequency ablation. Journal of cardiovascular electrophysiology. 1998; 9(11):1180–1185. [PubMed: 9835262]

21. Wutzler A, Huemer M, Parwani AS, Blaschke F, Haverkamp W, Boldt L-H. Contact force mapping during catheter ablation for atrial fibrillation: procedural data and one-year follow-up. Arch Med Sci. 2014; 10(2):266–272. [PubMed: 24904659]

22. Wakili R, Clauss S, Schmidt V, Ulbrich M, Hahnefeld A, Schüssler F, Siebermair J, Kääb S, Estner HL. Impact of real-time contact force and impedance measurement in pulmonary vein isolation procedures for treatment of atrial fibrillation. Clinical Research in Cardiology. 2014; 103(2):97–106. [PubMed: 24096555]

23. Martinek M, Lemes C, Sigmund E, Derndorfer M, Aichinger J, Winter S, NESSER H-J, Puererfellner H. Clinical impact of an open-irrigated radiofrequency catheter with direct force measurement on atrial fibrillation ablation. Pacing and Clinical Electrophysiology. 2012; 35(11):1312–1318. [PubMed: 22946636]

24. Natale A, Reddy VY, Monir G, Wilber DJ, Lindsay BD, McElderry HT, Kantipudi C, Mansour MC, Melby DP, Packer DL, et al. Paroxysmal AF catheter ablation with a contact force sensing catheter: results of the prospective, multicenter SMART-AF trial. Journal of the American College of Cardiology. 2014; 64(7):647–656. [PubMed: 25125294]

25. Surapaneni R, Guo Q, Xie Y, Young D, Mastrangelo CH. A three-axis high-resolution capacitive tactile imager system based on floating comb electrodes. Journal of Micromechanics and Microengineering. 2013; 23(7):075004.

26. Liao K, Hou MT, Yeh JA. A dielectiric liquid-based capcitive tactile sensor for normal and shear force sensing. Solid-State Sensors, Actuators and Microsystems (TRANSDUCERS & EUROSENSORS XXVII), 2013 Transducers & Eurosensors XXVII: The 17th International Conference on IEEE. 2013:1000–1003.

27. Takao H, Yawata M, Sawada K, Ishida M. A multifunctional integrated silicon tactile imager with arrays of strain and temperature sensors on single crystal silicon diaphragm. Sensors and Actuators A: Physical. 2010; 160(1):69–77.

28. Dobrzynska JA, Gijs M. Polymer-based flexible capacitive sensor for three-axial force measurements. Journal of Micromechanics and Microengineering. 2012; 23(1):015009.

29. Lee H-K, Chung J, Chang S-I, Yoon E. Real-time measurement of the three-axis contact force distribution using a flexible capacitive polymer tactile sensor. Journal of Micromechanics and Microengineering. 2011; 21(3):035010.

30. Pang C, Lee G-Y, Kim T-i, Kim SM, Kim HN, Ahn S-H, Suh K-Y. A flexible and highly sensitive strain-gauge sensor using reversible interlocking of nanofibres. Nature materials. 2012; 11(9):795–801. [PubMed: 22842511]

31. Mannsfeld SC, Tee BC, Stoltenberg RM, Chen CVH, Barman S, Muir BV, Sokolov AN, Reese C, Bao Z. Highly sensitive flexible pressure sensors with microstructured rubber dielectric layers. Nature materials. 2010; 9(10):859–864. [PubMed: 20835231]

32. Yamada T, Hayamizu Y, Yamamoto Y, Yomogida Y, Izadi-Najafabadi A, Futaba DN, Hata K. A stretchable carbon nanotube strain sensor for human-motion detection. Nature nanotechnology. 2011; 6(5):296–301.

33. Cohen DJ, Mitra D, Peterson K, Maharbiz MM. A highly elastic, capacitive strain gauge based on percolating nanotube networks. Nano letters. 2012; 12(4):1821–1825. [PubMed: 22409332]

34. Lu N, Lu C, Yang S, Rogers J. Highly sensitive skin-mountable strain gauges based entirely on elastomers. Advanced Functional Materials. 2012; 22(19):4044–4050.

35. Takizawa H, Tosaka H, Ohta R, Kaneko S, Ueda Y. Development of a microfine active bending catheter equipped with MIF tactile sensors. Micro Electro Mechanical Systems, 1999 MEMS'99 Twelfth IEEE International Conference on IEEE. 1999:412–417.

36. Valdastri P, Harada K, Menciassi A, Beccai L, Stefanini C, Fujie M, Dario P. Integration of a miniaturised triaxial force sensor in a minimally invasive surgical tool. Biomedical Engineering, IEEE Transactions on. 2006; 53(11):2397–2400.

37. Valdastri P, Houston K, Menciassi A, Dario P, Sieber A, Yanagihara M, Fujie M. Miniaturized cutting tool with triaxial force sensing capabilities for minimally invasive surgery. Journal of Medical Devices. 2007; 1(3):206–211.

38. Neuzil P, Wong CC, Reboud J. Electrically controlled giant piezoresistance in silicon nanowires. Nano letters. 2010; 10(4):1248–1252. [PubMed: 20192246]

39. Folch A, Toner M. Cellular micropatterns on biocompatible materials. Biotechnology progress. 1998; 14(3):388–392. [PubMed: 9622519]

40. Lee H-K, Chang S-I, Kim K-H, Yun K-S, Yoon E, Kim K-H. A modular expandable tactile sensor using flexible polymer. Micro Electro Mechanical Systems, 2005 MEMS 2005 18th IEEE International Conference on IEEE. 2005:642–645.

41. Mi Y, Chan Y, Trau D, Huang P, Chen E. Micromolding of PDMS scaffolds and microwells for tissue culture and cell patterning: A new method of microfabrication by the self-assembled micropatterns of diblock copolymer micelles. Polymer. 2006; 47(14):5124–5130.

42. Armani D, Liu C, Aluru N. Re-configurable fluid circuits by PDMS elastomer micromachining. Micro Electro Mechanical Systems, 1999 MEMS'99 Twelfth IEEE International Conference on Ieee. 1999:222–227.

43. Skotheim, TA., Reynolds, J. Handbook of Conducting Polymers, 2 Volume Set. CRC press; 2007.

44. Kirchmeyer S, Reuter K. Scientific importance, properties and growing applications of poly (3, 4-ethylenedioxythiophene). Journal of Materials Chemistry. 2005; 15(21):2077–2088.

45. Sotzing GA, Briglin SM, Grubbs RH, Lewis NS. Preparation and properties of vapor detector arrays formed from poly (3, 4-ethylenedioxy) thiophene-poly (styrene sulfonate)/insulating polymer composites. Analytical chemistry. 2000; 72(14):3181–3190. [PubMed: 10939385]

46. Lang U, Rust P, Dual J. Towards fully polymeric MEMS: Fabrication and testing of PEDOT/PSS strain gauges. Microelectronic Engineering. 2008; 85(5):1050–1053.

47. Daoud WA, Xin JH, Szeto YS. Polyethylenedioxythiophene coatings for humidity, temperature and strain sensing polyamide fibers. Sensors and Actuators B: Chemical. 2005; 109(2):329–333.

48. Sylgard 184 silicone elastomer kit. http://www.dowcorning.com/applications/search/default.aspx?R=131EN, (Accessed on 10/11/2016)

49. Park Y-L, Chen B-R, Wood RJ. Design and fabrication of soft artificial skin using embedded microchannels and liquid conductors. Sensors Journal, IEEE. 2012; 12(8):2711–2718.

50. Di Biase L, Natale A, Barrett C, Tan C, Elayi CS, Ching CK, Wang P, AL-AHMAD A, Arruda M, Burkhardt JD, et al. Relationship between catheter forces, lesion characteristics, "popping," and char formation: experience with robotic navigation system. Journal of cardiovascular electrophysiology. 2009; 20(4):436–440. [PubMed: 19017335]

51. Neumann T. Determining the elastic modulus of biological samples using atomic force microscopy. JPK Instruments Application Report. 2008:1–9.

52. Mirsky I, Parmley WW. Assessment of passive elastic stiffness for isolated heart muscle and the intact heart. Circulation research. 1973; 33(2):233–243. [PubMed: 4269516]

53. Kim Y-H, Marom EM, Herndon JE, McAdams HP. Pulmonary vein diameter, cross-sectional area, and shape: CT analysis 1. Radiology. 2005; 235(1):43–49. [PubMed: 15731371]

54. Clancy, LJ. Aerodynamics. Halsted Press; 1975.

55. Klingensmith, ME., et al. The Washington manual of surgery. Lippincott Williams & Wilkins; 2008.

56. Rausch J, Salun L, Griesheimer S, Ibis M, Werthschützky R. Printed piezoresistive strain sensors for monitoring of light-weight structures. 2011
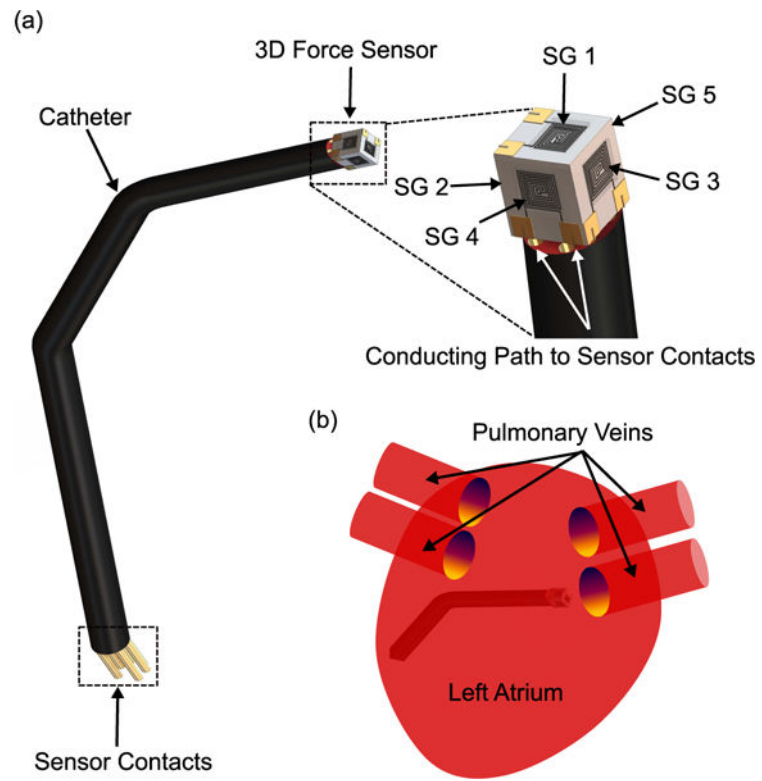
Fig. 1.
(a) Schematic diagrams of a catheter with the proposed 3D flexible force sensor. (b) Conceptual view of steering the catheter near pulmonary veins during ablation.
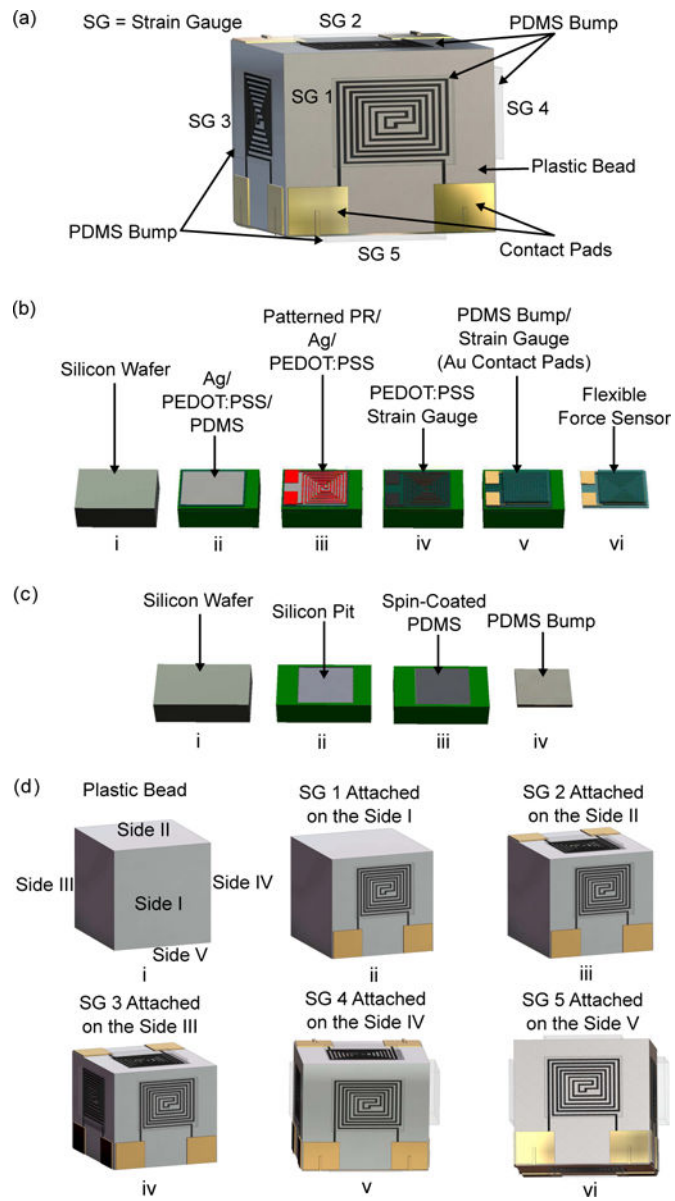
Fig. 2.
Schematic diagrams: (a) Proposed 3D flexible force sensor, (b) Process flow for the strain gauge on PDMS, (c) Process flow for the PDMS bump, and (d) Process flow for attaching the strain gauge with PDMS onto a cubic plastic bead. Side IV and side V are opposite to side III and side II, respectively.
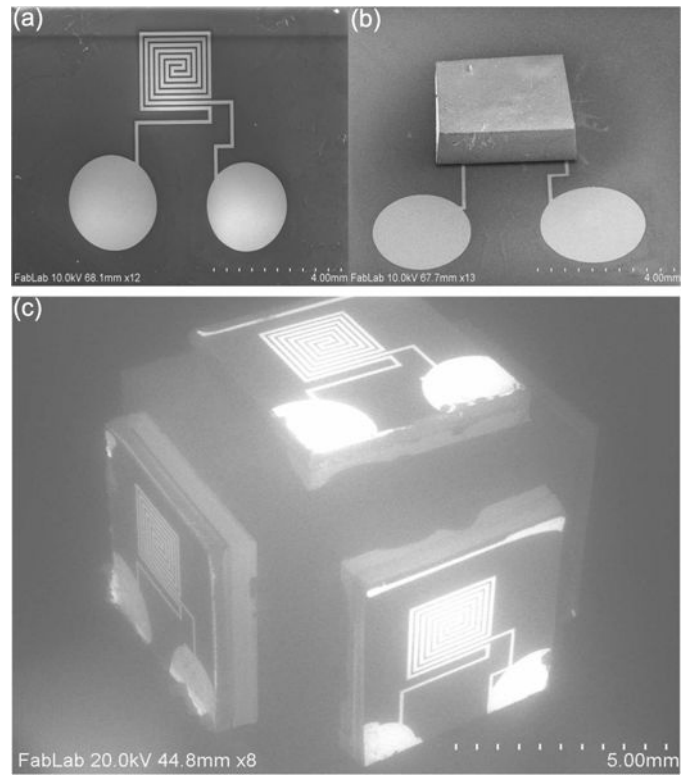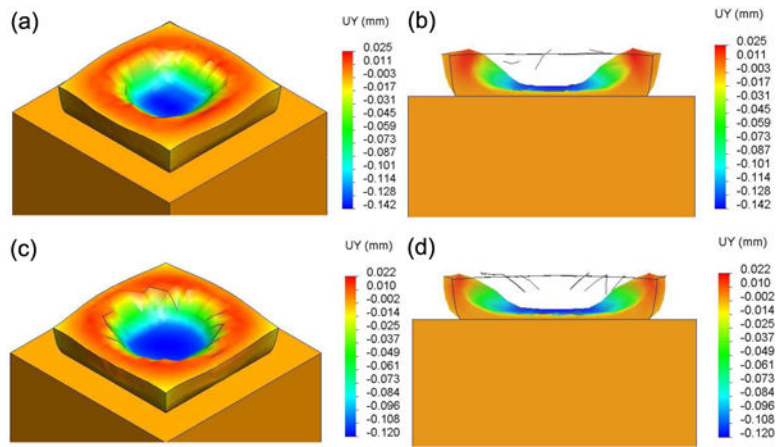
Fig. 3.
SEM images: (a) Strain gauge on the PDMS substrate without the PDMS bump, (b) Strain gauge on the PDMS substrate with the PDMS bump, and (c) 3D force sensor without PDMS bumps.
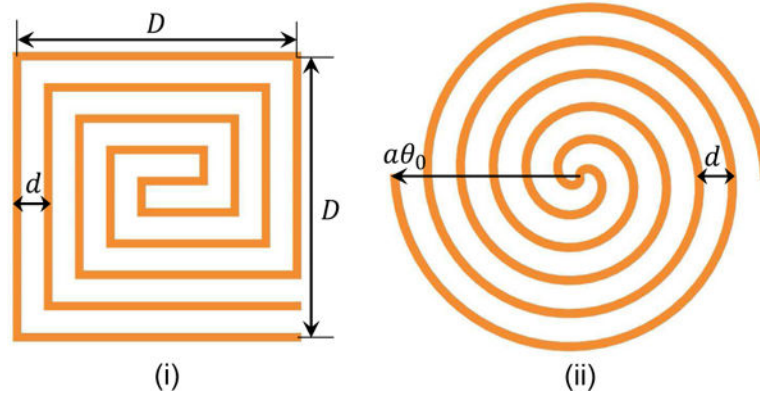
Fig. 4.
Schematic diagrams of two strain gauges made of square spirals (i) and circular spirals (ii), respectively.

Fig. 5.
Simulation results for the flexible force sensor under normal force: (a) Isometric view for pattern (i), (b) Cross-section view through vertex for pattern (i), (c) Isometric view for pattern (ii), and (d) Cross-section view through vertex for pattern (ii).
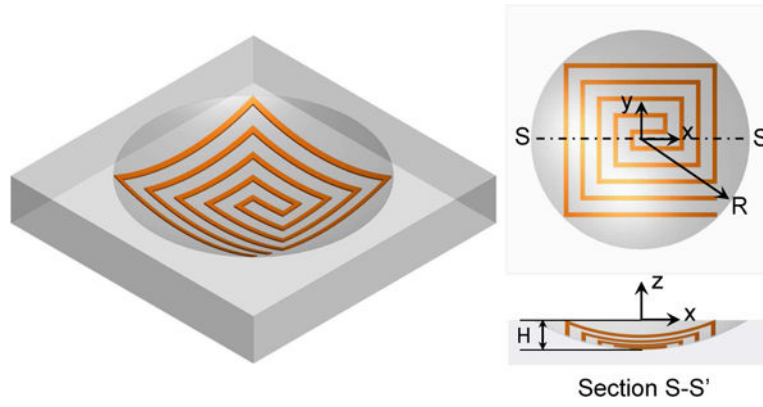
Fig. 6.
Schematic diagrams of the deformed strain gauge with pattern (i) on the PDMS substrate without the PDMS bump.
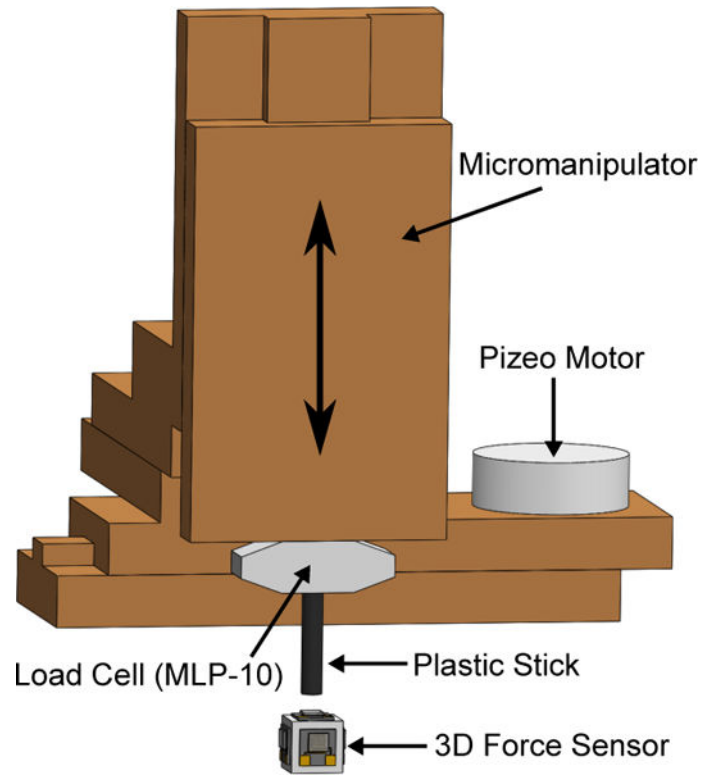
Fig. 7.
Schematic diagram of the calibration setup for the fabricated 3D force sensor.
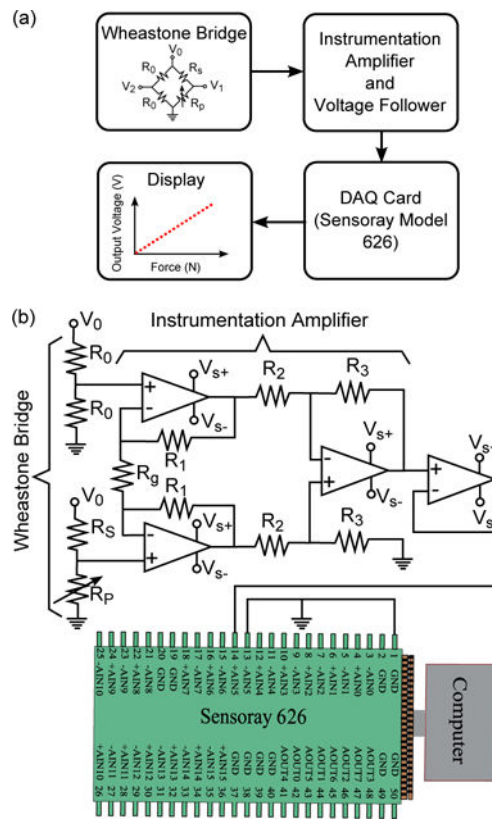
Fig. 8.
(a) Block diagram of the contact force sensing system. (b) Circuit diagram including the Wheatstone bridge circuit, electronic conditioning, and DAQ card. R_S and R_P represent the resistance of the fabricated strain gauge and the potentiometer, respectively.
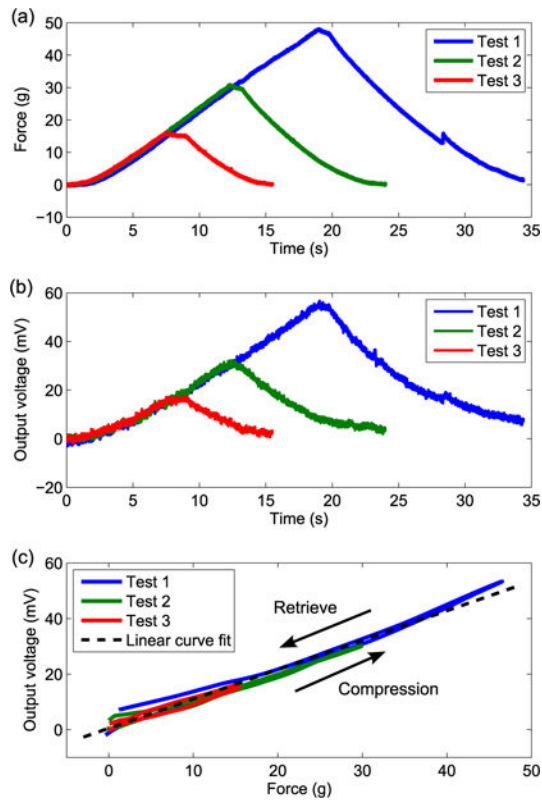
Fig. 9.
Calibration results for the fabricated flexible force sensor: (a) Compressive force measured by the commercial load cell versus time, (b) Output voltage of the fabricated flexible force sensor versus time, and (c) Output voltage of the fabricated flexible force sensor versus the compressive force measured by the commercial load cell. In tests 1, 2, and 3, the maximum displacements were 400 μm, 600 μm, and 900 μm, respectively.
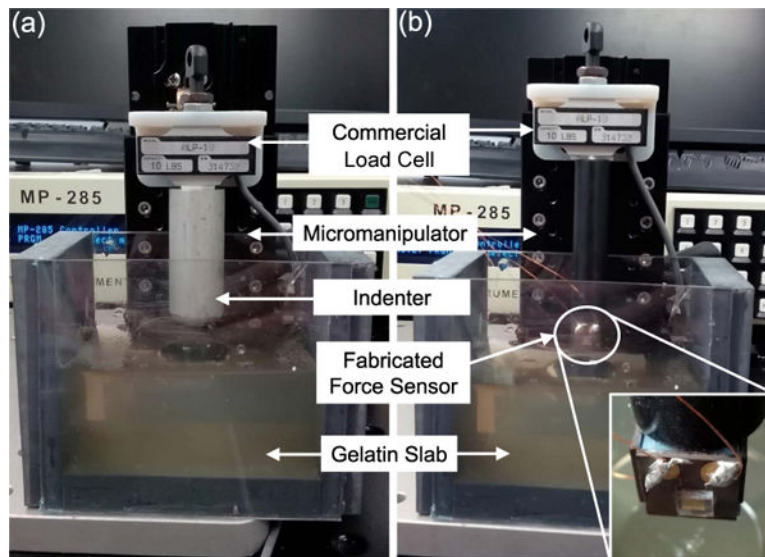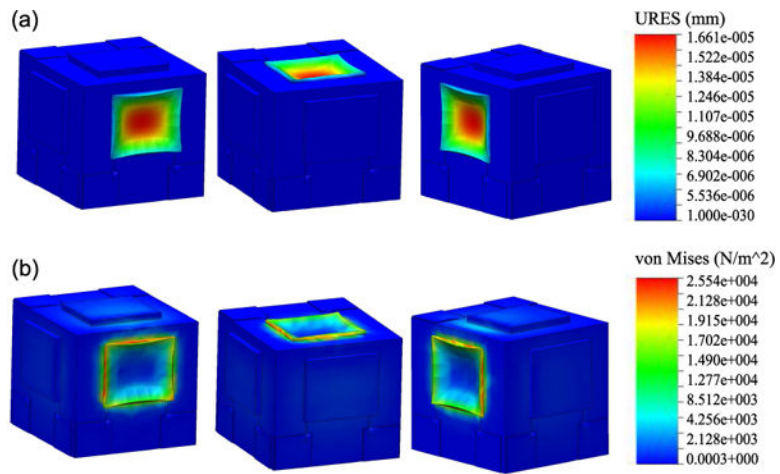
Fig. 10.
Experimental setup for the gelatin tests: (a) Measuring the stiffness of the gelatin slab and (b) Pressing the fabricated 3D force sensor against the gelatin tissue.
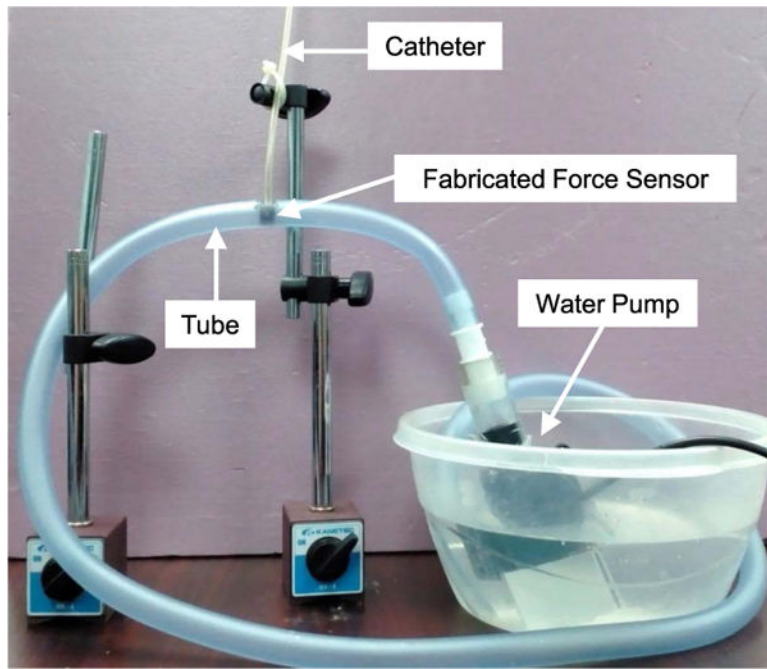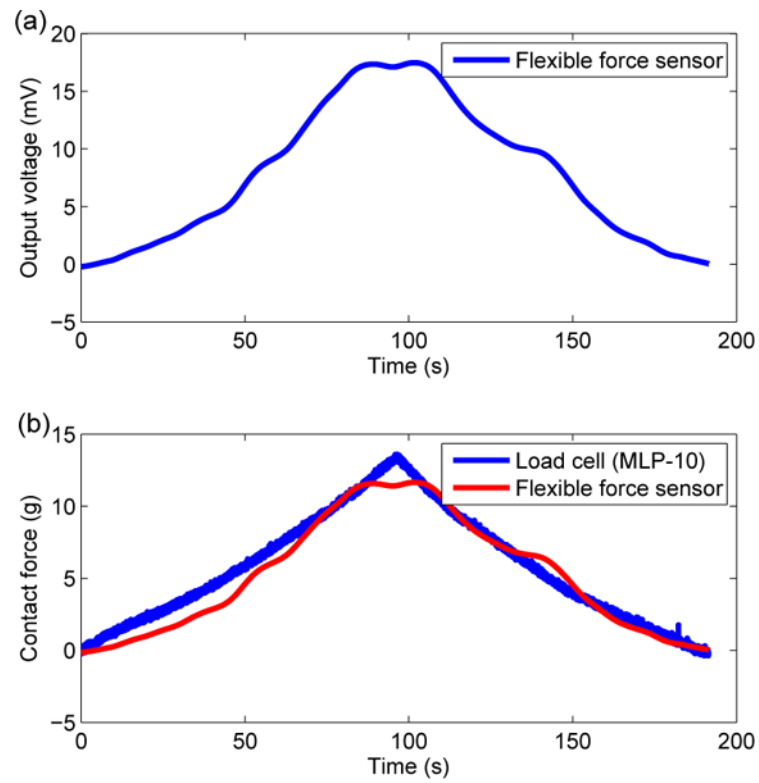
Fig. 11.
Experimental setup for testing the fabricated 3D force sensor in the presence of deionized water flow.

Fig. 12.
Simulation results of the 3D force sensor with PDMS bumps under 0.5N normal force: (a) Displacements of the flexible force sensors and (b) Stress distribution on the flexible force sensors.

Fig. 13.
Experimental results of the gelatin test with the PDMS bump: (a) Output voltage of the fabricated flexible force sensor and (b) Contact force measured by the commercial load cell and the fabricated flexible force sensor.
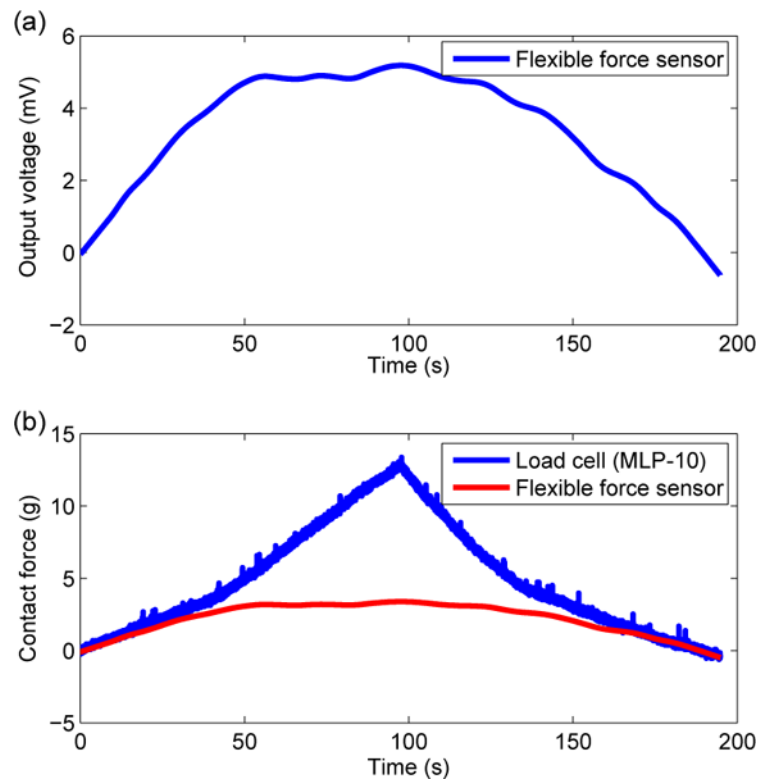
Fig. 14.
Experimental results of the gelatin test without the PDMS bump: (a) Output voltage of the fabricated flexible force sensor and (b) Contact force measured by the commercial load cell and the fabricated flexible force sensor.
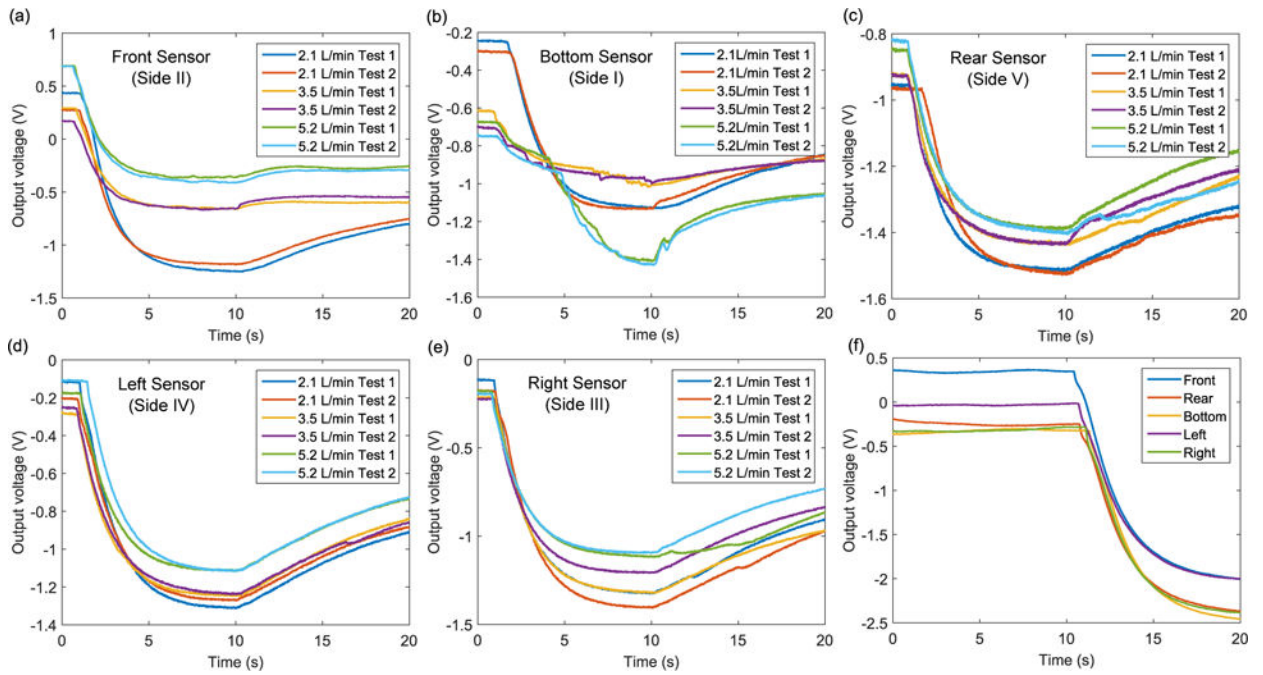
Fig. 15.
(a)–(e) Experimental results of the evaluation tests within the water flow (2.1 L/min, 3.5 L/min, and 5.2 L/min) for the front (a), bottom (b), rear (c), left (d), and right (e) flexible force sensors. The sensor on side II (see Fig. 2) faces the water flow, so the sensors on side I, II, III, IV, and V (see Fig. 2) are the bottom, front, right, left, and rear sensors, respectively. The water flow was supplied for 10s followed by a rest period of 10s. At each flow rate, two individual tests (Test 1 and Test 2) were performed. (f) The voltage output change after the sensors were immersed into the still water.

TABLE I

Comparison of Theoretical Sensitivity

p (MPa)	0.05	0.10	0.15	0.20
GF_i (MPa^{-1})	0.0049	0.0097	0.0149	0.0197
GF_{ii} (MPa^{-1})	1.2501e-4	2.8516e-4	4.2827e-4	5.7864e-4